J Adv Ceram

Research Article

Engineering oxygen vacancies via liquid reduction for superior lithium storage in rock-salt high-entropy oxide

Shibiao Xu[1,†], Zhengbing Wei[1,†], Meiyi Pan[1], Feilong Yin[1], Saisai Li[1], Cuihong Zheng[1], Na Lin[1], Aiqin Mao[1,2,✉], Xuefeng Liu[3,✉]

Cite this article: Xu SB, Wei ZB, Pan MY, et al. *J Adv Ceram* 2026, **15**(7): 9221328. https://doi.org/10.26599/JAC.2026.9221328

ABSTRACT: High-entropy oxides (HEOs) have attracted considerable attention for energy storage applications due to their structural stability and chemical versatility. However, their intrinsically low electrical conductivity remains a major obstacle to the practical application. In this work, oxygen-deficient rock-salt-type $(Co_{0.2}Cu_{0.2}Mg_{0.2}Ni_{0.2}Zn_{0.2})O$ HEOs were synthesized via a solution combustion method and subsequently reduced with H_2O_2 and $NaBH_4$ solution. The introduction of oxygen vacancies effectively accelerates charge transfer, enhances electron/Li^+ transport kinetics, and provides a higher pseudocapacitive contribution, all of which lead to improved electrochemical properties. As a result, $NaBH_4$-reduced $(Co_{0.2}Cu_{0.2}Mg_{0.2}Ni_{0.2}Zn_{0.2})O$ (HEO–$NaBH_4$) delivers an exceptional reversible capacity of 802 mAh·g^{-1} after 300 cycles at 0.2 A·g^{-1}, which is ~2.3 times that of the pristine sample. Even after 500 cycles at 1 A·g^{-1}, it retains 319 mAh·g^{-1}, a 45% improvement. Further insight into the lithium storage mechanism shows that the inherent lattice stability of HEO–$NaBH_4$ greatly hinders structural degradation and facilitates reversible redox reactions. This defect engineering route suggests potential applicability to other analogous materials.

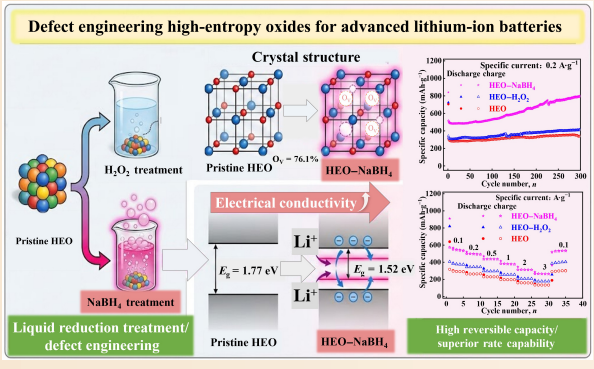

KEYWORDS: high-entropy oxides; lithium-ion battery; liquid reduction; oxygen vacancies; reaction kinetics

1 Introduction

Driven by the rising demand for higher energy density, improved safety, and better sustainability in energy storage, conventional anode materials such as graphite are increasingly insufficient for next-generation lithium-ion batteries (LIBs) [1]. This has spurred extensive research into alternative anode materials. For example, silicon/carbon anodes offer high capacity but suffer from severe volume expansion, leading to rapid capacity degradation and poor cycling stability [2]. In contrast, high-entropy oxides (HEOs), a new class of single-phase materials composed of five or more elements in near-equimolar ratios, have emerged as promising LIB anode candidates [3–7]. The high-entropy design is underpinned by four core effects, namely, high configurational entropy, severe lattice distortion, sluggish diffusion, and cocktail effects. These effects act synergistically to enhance structural stability and promote favorable ion/electron transport kinetics, leading to significantly improved electrochemical performance compared with conventional transition-metal oxides.

To further enhance the lithium-ion storage performance of HEOs, various strategies have been explored, including morphological, compositional, distortion, and vacancy engineering. Among these, introducing positively charged oxygen vacancies (O_V) has proven effective, as O_V increases electronic conductivity, improves electron/ion diffusion kinetics, and provides additional active sites for surface redox kinetics [8–10]. Several methods have been developed to create O_V into HEOs, such as cation/anion doping, low-temperature plasma treatment, high-temperature vacuum treatment, and high-temperature gas-phase reduction (e.g., H_2 and CO) [11–15]. For instance, Liu *et al.* [11] reported a Li^+-incorporated (LiCoCuMgNiZn)O HEO anode with tailored O_V, delivering a significantly improved rate capability (301 mAh·g^{-1} at 5 A·g^{-1}) and long-cycling stability (417 mAh·g^{-1} at 1 A·g^{-1} after 300 cycles). However, doping inevitably introduces foreign elements whose individual electrochemical influence is difficult to decouple. Similarly, Ozgur *et al.* [13] employed high-temperature vacuum treatment to tailor O_V in spinel $(FeCrCoMnZn)_3O_{4-\delta}$ HEO, achieving a peak

† Shibiao Xu and Zhengbing Wei contributed equally to this work.

[1] Advanced Ceramics Research Center, School of Materials Science and Engineering, Anhui University of Technology, Ma'anshan 243032, China. [2] Anhui Province Key Laboratory of Efficient Conversion and Solid-State Storage of Hydrogen & Electricity, Anhui University of Technology, Ma'anshan 243002, China. [3] College of Chemistry and Pharmaceutical Engineering, Nanyang Normal University, Nanyang 473061, China.

✉ Corresponding authors. E-mail: A. Mao, maoaiqin@ahut.edu.cn; X. Liu, liuxuefeng@nynu.edu.cn

Received: March 16, 2026; Revised: May 6, 2026; Accepted: May 27, 2026

power density of 102 mW·cm^{-2}, a specific capacity of 576.07 mAh·g^{-1}, and a specific energy of 662.46 Wh·kg^{-1} at 5 mA·cm^{-2} in Zn–air batteries. Nevertheless, high-temperature treatment causes grain coarsening, along with safety risks, high costs, and high energy consumption, whereas plasma treatment involves similarly high safety and energy burdens but at an even greater expense. Therefore, low-temperature liquid reduction has emerged as a mild and efficient alternative to create O_V without altering the chemical composition or inducing grain coarsening [10,16].

Inspired by these considerations, we selected the representative rock-salt-type $(Co_{0.2}Cu_{0.2}Mg_{0.2}Ni_{0.2}Zn_{0.2})O$ HEO as a model system, where Co, Ni, and Zn offer redox activity, Mg provides structural integrity, and Cu enables an *in situ* conductive metallic network [17]. The anode materials were synthesized via solution combustion synthesis (SCS) and then treated with a mild reduction solution at room temperature to modulate O_V. To increase the O_V concentration, a strong reducing agent, sodium borohydride ($NaBH_4$), was employed. For comparison, hydrogen peroxide (H_2O_2), typically an oxidant, was also used as a mild reducing agent because the as-prepared pristine HEO already contains a certain amount of O_V that chemisorbs H_2O_2 and triggers Fenton-like reactions (e.g., $Co^{3+} + H_2O_2 \rightarrow Co^{2+} + \cdot OOH + H^+$ and $Ni^{3+} + H_2O_2 \rightarrow Ni^{2+} + \cdot OOH + H^+$) [18]. The introduced O_V substantially enhanced lithium-storage performance, delivering fast kinetics and high capacity [19,20]. This work thus demonstrates the effectiveness of low-temperature defect engineering for optimizing rock-salt HEOs and offers valuable insights into designing high-performance LIB anodes.

2 Experimental

2.1 Materials synthesis

Rock-salt-type $(Co_{0.2}Cu_{0.2}Mg_{0.2}Ni_{0.2}Zn_{0.2})O$ powders were synthesized via the reported SCS method [21–23] and subsequently reduced with H_2O_2 and $NaBH_4$ solution, as illustrated in Fig. 1(a). For the standard synthesis, equimolar amounts (1.250 mmol each) of $Co(NO_3)_2{\cdot}6H_2O$, $Cu(NO_3)_2{\cdot}3H_2O$, $Mg(NO_3)_2{\cdot}6H_2O$, $Ni(NO_3)_2{\cdot}6H_2O$, and $Zn(NO_3)_2{\cdot}6H_2O$ were dissolved in a small volume of deionized water, with glycine (3.472 mmol) added as the fuel. All chemical reagents were obtained from Sinopharm Chemical Reagent Co., Ltd. (China) and used without further purification. The resulting solution was continuously stirred and evaporated at 80 °C to form a homogeneous gel, which was subsequently transferred to an electric furnace and combusted rapidly at 900 °C for 30 min to

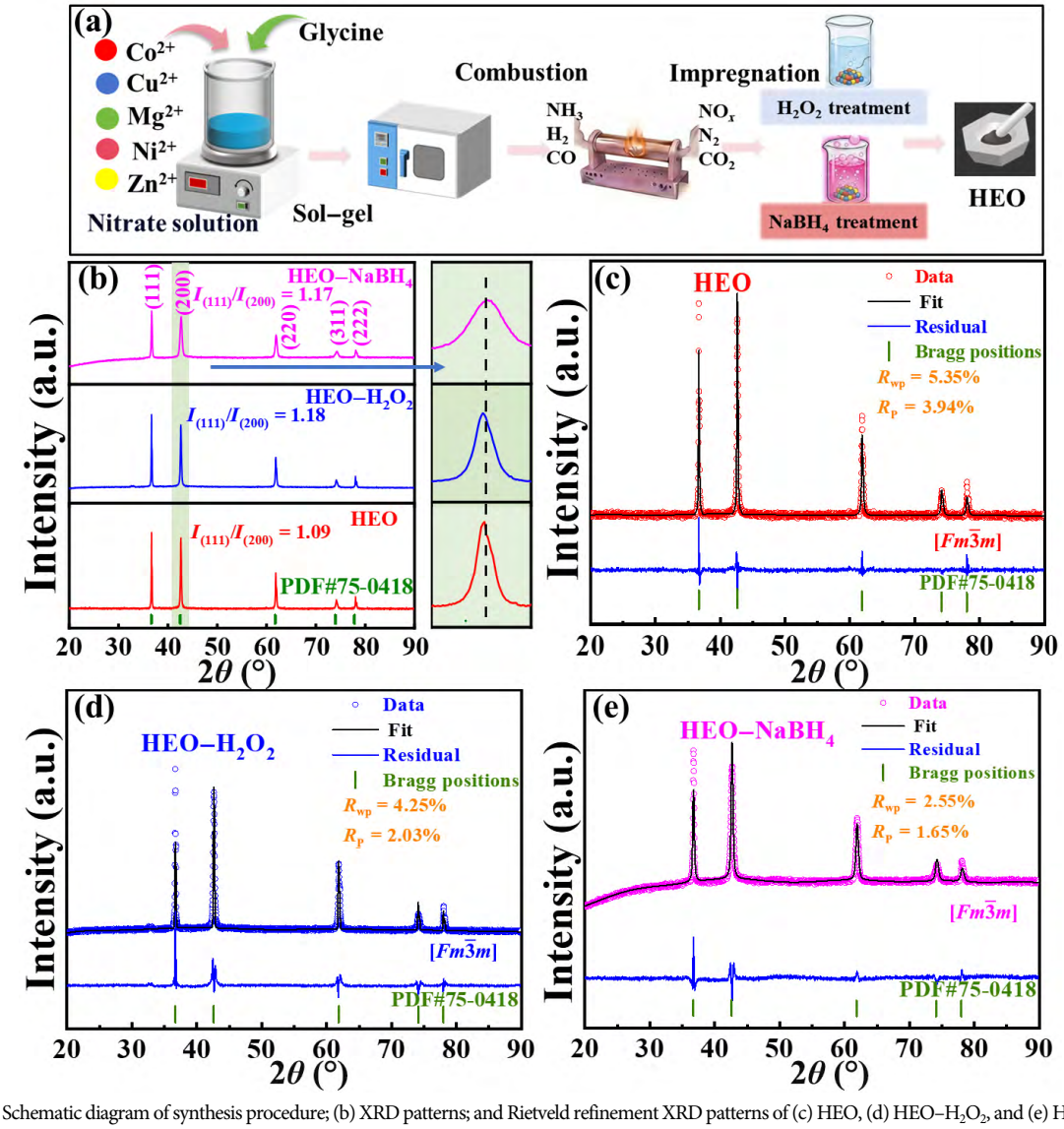

Fig. 1 (a) Schematic diagram of synthesis procedure; (b) XRD patterns; and Rietveld refinement XRD patterns of (c) HEO, (d) HEO–H_2O_2, and (e) HEO–$NaBH_4$.

yield rock-salt-type $(Co_{0.2}Cu_{0.2}Mg_{0.2}Ni_{0.2}Zn_{0.2})O$ powders. Finally, the resultant powders were further reduced by dispersing them in 25 mL of either 0.2 M $NaBH_4$ or 0.1 M H_2O_2 solution under mechanical stirring for 2 h to obtain O_V-rich $(Co_{0.2}Cu_{0.2}Mg_{0.2}Ni_{0.2}Zn_{0.2})O$ powders. The choice of 0.1 M H_2O_2 enables the reduced $(Co_{0.2}Cu_{0.2}Mg_{0.2}Ni_{0.2}Zn_{0.2})O$ to maintain a single rock-salt structure, while 0.2 M H_2O_2 results in $CoCu_2O_3$ impurities (Fig. S1 in the Electronic Supplementary Material (ESM)). After reduction, the samples were collected by centrifugation, washed repeatedly with deionized water, and dried at 80 °C for 12 h. For clarity, the as-synthesized sample and those reduced with $NaBH_4$ and H_2O_2 are denoted as HEO, HEO–$NaBH_4$, and HEO–H_2O_2, respectively.

2.2 Materials characterization

The phase composition of the samples was characterized by X-ray diffraction (XRD) using a MiniFlex 600 diffractometer (Rigaku, Japan) equipped with monochromatic Cu Kα radiation (λ = 1.5406 Å) operating at 40 kV and 40 mA. The obtained diffraction patterns were refined by the Rietveld method using the GSAS software package. The surface morphology and elemental distribution were examined using a scanning electron microscope (SEM; Sigma HV-01-043, Zeiss, Germany) coupled with an energy-dispersive X-ray spectrometer (EDS) system (Nano Xflash Detector 5010, Bruker, Germany). Transmission electron microscopy (TEM) images and selected area electron diffraction (SAED) patterns were obtained using an ultrahigh-resolution transmission electron microscope (HRTEM; JEM-2010, JEOL, Japan). The textural properties were evaluated through N_2 adsorption–desorption isotherms measured on a JW-BK200 analyzer (JWGB, China). The specific surface area and pore size distribution were derived using the Brunauer–Emmett–Teller (BET) and Barrett–Joyner–Halenda (BJH) models, respectively. The surface chemical states and oxygen defects were characterized by an X-ray photoelectron spectrometer (XPS; ESCALAB 250Xi, Thermo Fisher Scientific, USA). Electron paramagnetic resonance (EPR) spectra were acquired at room temperature on an X-band spectrometer (EMX-plus, Bruker, Germany). Electrical conductivity was measured at room temperature using a four-point probe system (RTS-4, 4Probes Tech. Co., Ltd., China), and optical absorption spectra were recorded on an ultraviolet–visible–near-infrared (UV–Vis–NIR) spectrophotometer (UV-3600, Shimadzu, Japan) within the wavelength range of 200–2500 nm. The optical band gap energy was subsequently estimated from the Tauc plots derived from the absorption spectra.

2.3 Electrochemical measurements

CR2025-type coin cells were assembled in an argon-filled glove box (Super-750, MIKROUNA, China; H_2O/O_2 < 0.01 ppm) to evaluate the lithium-ion storage performance. The working electrode was prepared by thoroughly grinding the HEO active material, conductive carbon black, and sodium alginate binder in a mass ratio of 7 : 2 : 1 to form a homogeneous slurry. This slurry was uniformly coated onto a clean copper foil and subsequently dried under vacuum at 60 °C for 24 h. After drying, the electrodes were punched into 12 mm discs and pressed under a pressure of 8 MPa for 30 s to achieve a mass loading of 1.0–1.6 mg·cm^{-2}. Lithium metal foil (15.6 mm in diameter) was used as the counter electrode, while a polypropylene (PP) porous membrane (ϕ19 mm; Canrd, China) served as the separator. The electrolyte consisted of 1 M $LiPF_6$ dissolved in a 1 : 1 : 1 (v/v/v) mixture of ethylene carbonate (EC), ethyl methyl carbonate (EMC), and dimethyl carbonate (DMC).

Galvanostatic charge–discharge tests and galvanostatic intermittent titration technique (GITT) measurements were conducted on a multichannel battery testing system (CT-4008T-5V10mA-64, Neware Technology Co., Ltd., China) within a potential window of 0.01–3.0 V (vs. Li^+/Li) at room temperature. The GITT protocol involved applying a constant-current discharge pulse of 100 mA·g^{-1} for 600 s, followed by an open-circuit relaxation period of 1200 s. Electrochemical impedance spectroscopy (EIS) and cyclic voltammetry (CV) measurements were performed using a CHI760E electrochemical workstation (Shanghai Chenhua Instruments Co., Ltd., China). EIS measurements were performed in the frequency range from 10^5 to 0.01 Hz, while CV curves were recorded at scan rates ranging from 0.1 to 1.0 mV·s^{-1} within the same potential range.

3 Results and discussion

3.1 Structure characterization

The XRD patterns of the three as-synthesized samples are shown in Fig. 1(b). All three samples exhibit nearly identical diffraction peaks, which closely align with the reference pattern of rock-salt CoO (PDF #75-0418), confirming that each sample adopts a single-phase rock-salt structure [9]. Notably, slight shifts in peak positions and minor variations in peak intensities are observed in the standard pattern, which are attributed to the solid solubility of five metal cations within the rock-salt lattice. Furthermore, the magnified view of Fig. 1(b) reveals that the (200) diffraction peak of the HEO–$NaBH_4$ sample shifts toward a higher angle, while that of the HEO–H_2O_2 sample shifts slightly to a lower angle. This indicates a contraction and an expansion of the lattice parameter, respectively, which can be attributed to the interplay between O_V concentration and cation valence changes during charge compensation [10,11]. To precisely quantify these microstructural changes, Rietveld refinement was performed, as shown in Figs. 1(c)–1(e). Detailed parameters are provided in Table S1 in the ESM. Both the weighted profile R-factor (R_{wp}) and the profile R-factor (R_p) are below 10%, demonstrating the reliability of the refinements. The refined lattice parameters ($a = b = c$) for the HEO, HEO–H_2O_2, and HEO–$NaBH_4$ samples are 4.237, 4.240, and 4.234 Å, respectively, which are consistent with the observed shift in the (200) diffraction peak.

It has been reported that the degree of lattice distortion in rock-salt HEOs can be evaluated by the intensity ratio of the (111) and (200) peaks, denoted as $I_{(111)}/I_{(200)}$. For an ideal rock-salt lattice, the $I_{(111)}/I_{(200)}$ ratio is approximately 0.67 [24]. In this study, the calculated $I_{(111)}/I_{(200)}$ ratios for the HEO, HEO–H_2O_2, and HEO–$NaBH_4$ samples are 1.09, 1.18, and 1.17, respectively, indicating significant lattice distortion in all samples. Such lattice distortion is primarily driven by the Jahn–Teller effect of Cu^{2+} ions [9]. Notably, the slightly increased $I_{(111)}/I_{(200)}$ ratio after reduction treatment signifies aggravated distortion, a consequence of the increased Cu^{2+} content that is definitively verified by subsequent XPS analysis. The enhanced lattice distortion of HEO–H_2O_2 and HEO–$NaBH_4$ provides abundant ion transport pathways to improve electrochemical performance [25]. In addition, the average crystallite size is calculated using the Scherrer equation, $D = K\lambda/(\beta\cos\theta)$, where D is the crystallite size (nm), K is the Scherrer constant (0.9), λ is the wavelength, and β and θ represent the full width at half maximum (FWHM) and the Bragg diffraction angle, respectively. The calculated crystallite sizes for HEO, HEO–H_2O_2, and HEO–$NaBH_4$ are 44.10, 42.97, and 26.50 nm, respectively. The notable refinement of crystallites in the HEO–$NaBH_4$ sample is expected to shorten Li^+ diffusion

pathways and alleviate stress concentration during cycling, thereby contributing to enhanced rate capability and cycling stability [26].

Figure 2 displays the morphological and microstructural features of the as-synthesized samples. All samples exhibit a porous network structure (Figs. 2(a1)–2(c2)), indicating that the original morphology of the pristine HEO is well preserved after chemical reduction treatment. The corresponding EDS mappings of HEO–$NaBH_4$ (Fig. 2(d)) confirm a homogeneous distribution of all constituent elements at the microscale, with no evidence of phase segregation or elemental agglomeration. Furthermore, the TEM image of HEO–$NaBH_4$ (Fig. 2(e)) reveals a porous architecture, while the corresponding SAED pattern (Fig. 2(f)) exhibits well-defined diffraction rings indexed to the (111), (200), (220), and (311) planes of the rock-salt structure, confirming its polycrystalline nature. Moreover, the HRTEM image (Fig. 2(g)) displays well-resolved lattice fringes with a measured interplanar distance of 2.38 Å, corresponding to the (111) plane of the rock-salt structure. Additionally, localized lattice distortions are evident, which can be associated with the elevated concentration of oxygen vacancies induced during $NaBH_4$ reduction.

N_2 adsorption–desorption analysis was conducted to evaluate the porosity of the three samples (Figs. S2(a)–S2(c) in the ESM). The obtained isotherms for all samples exhibit a typical type-IV profile, characteristic of mesoporous structures. The detailed textural parameters derived from the measurements are summarized in Table S2 in the ESM. Owing to their similar porous morphologies, the specific surface area (S_{BET}), pore volume (V_{BJH}), average pore size (D_{aver}), and most probable pore size (D_{most}) of the three samples are comparable. Notably, after chemical reduction, both the HEO–H_2O_2 and HEO–$NaBH_4$ samples show a discernible increase in pore volume and a broadening of pore size relative to pristine HEO. Such a tailored pore architecture is advantageous for electrolyte infiltration, which improves Li^+ accessibility and reduces Li^+ transport resistance. Furthermore, the enlarged pore volume can effectively accommodate volume variations during lithiation/delithiation processes, thereby mitigating mechanical strain and improving structural integrity over extended cycling.

The surface elemental composition and chemical states of the samples were investigated by XPS. The survey spectra (Fig. S3(a) in the ESM) confirm the coexistence of Mg, Cu, Zn, Ni, Co, and O in all samples, which is consistent with the EDS mapping results. The high-resolution Cu 2p spectra (Fig. 3(b)) display characteristic peaks at 934.1 eV (Cu $2p_{3/2}$) and 954.0 eV (Cu $2p_{1/2}$) corresponding to Cu^{2+} and peaks at 932.4 eV (Cu $2p_{3/2}$) and 952.2 eV (Cu $2p_{1/2}$) corresponding to Cu^+, indicating the coexistence of Cu^{2+} and Cu^+ species [27]. Similarly, the Co 2p and Ni 2p spectra (Figs. 3(a) and 3(c)) confirm that Co and Ni exist in mixed +2 and +3 valence states, while Mg and Zn remain exclusively divalent (Figs. S3(b) and S3(c) in the ESM) [28,29]. Furthermore, the quantitative distribution of cation valence states is summarized in Fig. 3(e). Compared with pristine HEO, the relative content of high-valence Co^{3+} and Ni^{3+} in the HEO–$NaBH_4$ and HEO–H_2O_2 samples decreases significantly after reduction treatment. In contrast, the content of high-valence Cu^{2+} increases, which can be attributed to its ability to maintain a more stable configuration in the octahedral crystal field [30].

The high-resolution O 1s spectra in Fig. 3(d) can be fitted with three peaks located at 529.7, 531.6, and 533.4 eV, corresponding to lattice oxygen (O_L), O_V, and adsorbed oxygen (O_W), respectively [31–33]. Quantitative analysis based on the peak area reveals that the surface O_V concentration increases significantly from 31.4% in pristine HEO to 57.6% in HEO–H_2O_2 and reaches 76.1% in HEO–$NaBH_4$. This trend demonstrates that the reduction treatment effectively promotes oxygen release and generates abundant surface O_V, accompanied by the partial reduction of high-valence transition-metal ions. The substantially higher O_V concentration in HEO–$NaBH_4$ than that in HEO–H_2O_2 can be attributed to the stronger reduction ability of $NaBH_4$ [34]. Because XPS is inherently surface sensitive, EPR spectroscopy was employed to verify whether the bulk O_V concentration follows the same trend as its surface counterpart (Fig. 3(f)). Note that a prominent EPR signal at g = 2.003 (where g is the spectroscopic splitting factor) assigned to bulk O_V that perturbs electronic spin states is observed for all three samples, and its intensity scales positively with the bulk O_V concentration [35]. As expected, HEO–$NaBH_4$ displays the highest concentration of O_V, followed by HEO–H_2O_2 and HEO, which is consistent with the above O 1s XPS results. Based on the XPS and EPR results, oxygen vacancies are primarily distributed on the surface/near-surface region,

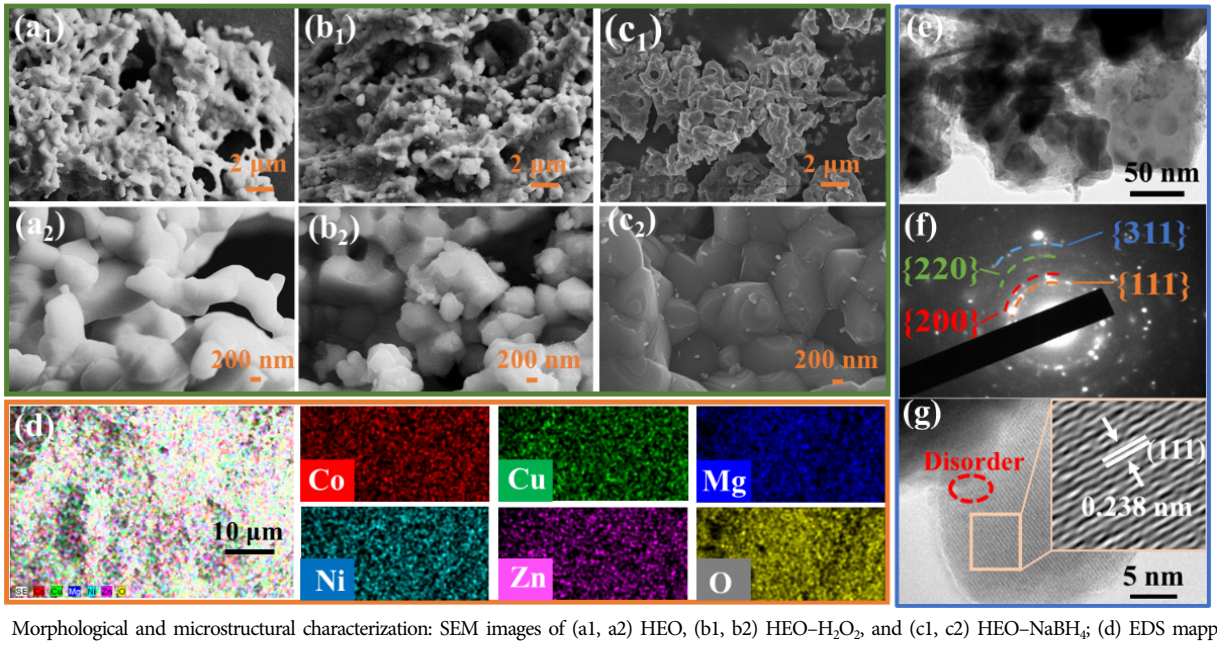

Fig. 2 Morphological and microstructural characterization: SEM images of (a1, a2) HEO, (b1, b2) HEO–H_2O_2, and (c1, c2) HEO–$NaBH_4$; (d) EDS mapping of HEO–$NaBH_4$; (e) TEM image, (f) SAED pattern, and (g) HRTEM image of HEO–$NaBH_4$.

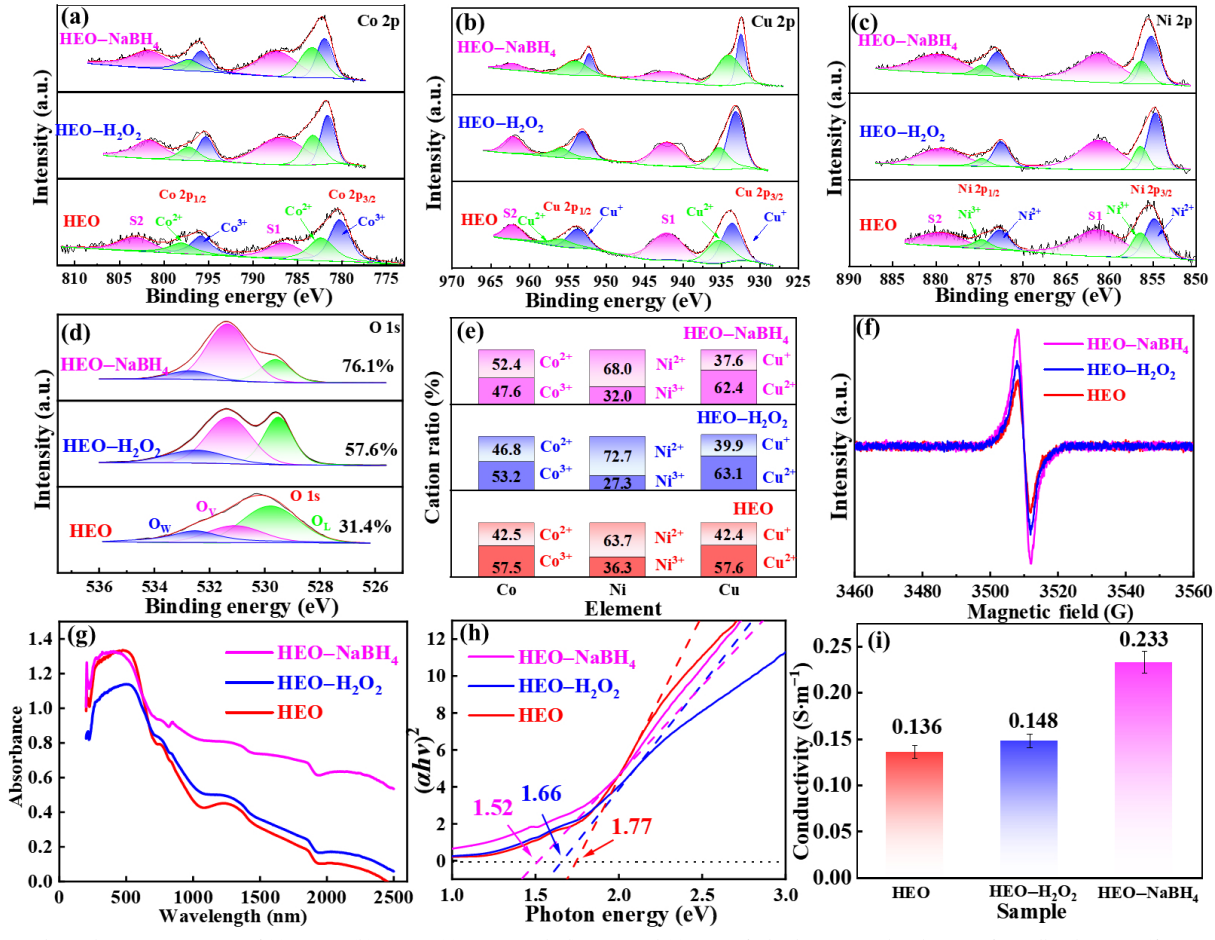

Fig. 3 High-resolution XPS spectra of (a) Co 2p, (b) Cu 2p, (c) Ni 2p, and (d) O 1s, and (e) quantified valence state distribution of metallic elements; (f) EPR spectra; (g) UV–Vis diffuse reflectance spectra and (h) corresponding $(\alpha h\nu)^2$ vs. $h\nu$ plots, α is absorbance, h is Planck's constant, and ν is the photon frequency; (i) electrical conductivity.

preferentially forming at oxygen sites coordinated with multivalent cations (e.g., Co and Ni). The observed decrease in Co^{3+} and Ni^{3+} contents upon reduction treatment confirms that O_V formation is accompanied by a decrease in cation valence states to achieve charge compensation.

Oxygen vacancies contribute to enhanced electrical conductivity, thereby facilitating faster electron transport during charge/discharge processes. This effect is further verified by the UV–Vis diffuse reflectance spectra (Fig. 3(g)). Within the measured wavelength range (200–2500 nm), HEO–$NaBH_4$ exhibits the strongest optical absorption, which is primarily attributed to its highest concentration of O_V induced by the strong reducing capability of $NaBH_4$. The optical band gaps of all three samples were further determined by the Tauc relation $[F(R_\infty)\cdot h\nu]^{1/n} = A(h\nu - E_g)$, where $F(R_\infty)$ is the Kubelka–Munk function; h is Planck's constant (6.63×10^{-34} J·s); ν is the photon frequency; A is a constant; E_g is the band gap energy; n = 1/2 for direct optical transitions in this study. The calculated band gap of HEO–$NaBH_4$ is 1.52 eV, which is considerably lower than those of HEO–H_2O_2 (1.66 eV) and pristine HEO (1.77 eV) (Fig. 3(h)). The reduction in band gap confirms the improvement in both intrinsic and extrinsic electronic conductivity. This is because the introduction of oxygen vacancies generates defect levels within the band gap, which effectively narrows the band gap, reduces charge–transfer resistance, and enhances electronic conduction [36]. The above spectroscopic findings align well with the directly measured electrical conductivity, as shown in Fig. 3(i). Owing to its highest O_V concentration, HEO–$NaBH_4$ exhibits the highest electronic conductivity of 0.233 $S\cdot m^{-1}$ among the three samples. This excellent conductive property facilitates fast electron transfer and reduces polarization during the charge storage process, thereby ensuring fast electronic transport kinetics and high power output. Generally, the introduction of oxygen vacancies not only modifies the electronic structure, thereby promoting fast electron transfer but also induces internal electric fields that facilitate Li^+ migration. Additionally, the unsaturated bonds created by oxygen vacancies on the electrode surface can provide more active sites for Li^+ adsorption.

3.2 Electrochemical performance

To investigate the effect of O_V on lithium storage, the electrochemical performance of HEO, HEO–H_2O_2, and HEO–$NaBH_4$ electrodes is evaluated in coin-type half cells. Figure 4(a) plots the first three cycles of CV curves for HEO–$NaBH_4$, alongside the first three dQ/dV profiles (Fig. 4(c) and Figs. S3(c) and S3(f) in the ESM). During the first cycle, a sharp reduction peak at approximately 0.61 V can be attributed to the gradual reduction of transition metal oxides to metal and the Li_2O matrix, while the formation of a solid electrolyte interface (SEI) film and Li–Zn alloy can be found at a lower voltage (0.40 V) [25]. An oxidation peak at approximately 1.72 V corresponds to the oxidation of metal species. After the first cycle, the reduction peak becomes significantly weaker and shifts to a higher potential, indicating a decrease in electrochemical polarization. It is worth noting that in subsequent cycles, only one pair of broad oxidation/reduction peaks is observed, suggesting

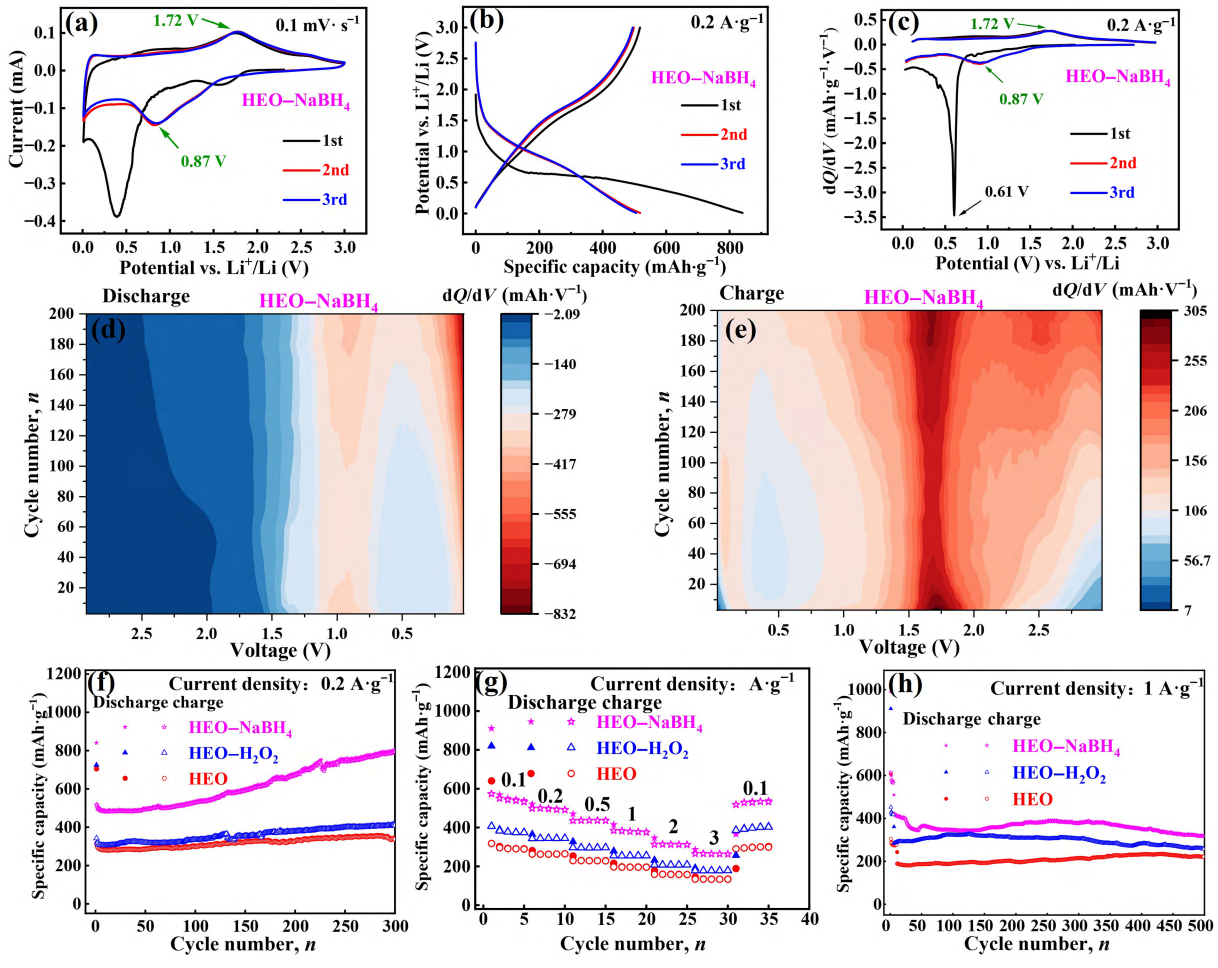

Fig. 4 Electrochemical performance of as-synthesized electrodes: (a) CV curves for the first three cycles at 0.1 mV·s^{-1}, (b) charge–discharge curves at 0.2 A·g^{-1}, (c) dQ/dV plots, and (d, e) contour plots of differential capacity (dQ/dV) vs. voltage over 200 cycles of HEO–$NaBH_4$ electrode; (f) cycling performance at 0.2 A·g^{-1}, (g) rate capability, and (h) long-term cycling performance at 1 A·g^{-1} after initial activation at 0.1 mA·g^{-1} for 5 cycles.

that both reactions occur gradually over a wide potential range. This behavior originates from the initial random distribution of cations, leading to well-mixed active elements at the atomic scale and thus facilitating structural optimization during cycling. Such structural characteristics facilitate the progressive optimization and stabilization of the electrode during cycling. The good overlap of the CV curves and the well-defined redox peaks in the dQ/dV profiles further confirm the good reversibility and cycling stability, which favors reversible Li^+ insertion and extraction. Similar features are observed for both HEO and HEO–H_2O_2 (Figs. S4(a), S4(d), S4(c), S4(e), and S4(f) in the ESM). The dominant lithium storage mechanism of rock-salt HEO is characteristic of conversion reactions, and the proposed electrochemical processes are shown in Reactions (1) and (2):

$$MO + 2Li^+ + 2e^- \leftrightarrow M + Li_2O \ (M = Co, Cu, Ni, \text{and } Zn) \quad (1)$$

$$Zn + Li^+ + e^- \leftrightarrow Li\text{-}Zn \quad (2)$$

The galvanostatic charge/discharge profiles of the synthesized electrodes at 0.2 A·g^{-1} during the first three cycles are shown in Fig. 4(b) and Figs. S4(b) and S4(e) in the ESM. The initial discharge/charge capacities of HEO–$NaBH_4$, HEO–H_2O_2, and HEO are 841/518, 725/343, and 705/316 mAh·g^{-1} with initial coulombic efficiencies (CE) of 61.55%, 47.26%, and 44.88%, respectively. Furthermore, the dQ/dV contour plots of the three electrodes from the 3rd to the 200th cycle are shown in Figs. 4(d) and 4(e) and Figs. S5(a)–S5(d) in the ESM. The darker the color of the peaks is, the greater the intensity and the higher the capacity of the batteries. Compared with the other two electrodes, the HEO–$NaBH_4$ electrode shows a notably stable peak position and intensity throughout cycling. This consistency indicates the formation of a robust SEI layer and highly reversible redox reactions during long-term cycling.

The cycling performance is first examined at a current density of 0.2 A·g^{-1} (Fig. 4(f)). The pristine HEO delivers a stable discharge capacity of 342 mAh·g^{-1} after 300 cycles, which aligns with the performance reported for rock-salt-type $(Co_{0.2}Cu_{0.2}Mg_{0.2}Ni_{0.2}Zn_{0.2})O$ synthesized by electrospinning [37]. In comparison, HEO–H_2O_2 shows an improved reversible capacity of 415 mAh·g^{-1}, whereas HEO–$NaBH_4$ achieves a markedly higher capacity of 802 mAh·g^{-1} after the same number of cycles, representing a 2.3-fold enhancement over the pristine sample. The superior performance of HEO–H_2O_2 and, more markedly, HEO–$NaBH_4$ over pristine HEO arises from the synergy among increased O_V concentration, enhanced lattice distortion, and favorable textural properties, with O_V being especially vital for boosting capacity and rate capability.

The rate performance is compared over current densities ranging from 0.1 to 3 A·g^{-1} in Fig. 4(g). At each rate, HEO–$NaBH_4$ displays the highest reversible capacity among the three electrodes, reflecting its superior Li^+ diffusion and reaction kinetics. For

example, when the current density increases from 0.1 to 3 A·g^{-1}, the average discharge specific capacities of HEO, HEO–H_2O_2, and HEO–$NaBH_4$ drop from 292, 378, and 545 mAh·g^{-1} to 136, 181, and 270 mAh·g^{-1}, respectively. Upon returning to 0.1 A·g^{-1}, the capacity recovers effectively, indicating excellent structural stability and reversibility of the electrodes. Furthermore, the long-term cycling performance was evaluated at a high current density of 1 A·g^{-1}, following an initial activation at 0.1 A·g^{-1} for 5 cycles (Fig. 4(h)). The HEO–$NaBH_4$ electrode maintains the highest capacity of 319 mAh·g^{-1} after 500 cycles, representing a 24% and 45% improvement over the HEO–H_2O_2 (257 mAh·g^{-1}) and pristine HEO electrodes (223 mAh·g^{-1}), respectively. The slightly lower capacity observed at high current density may be attributed to the continuous activation and SEI formation during cycling. In comparison with previously reported results, the optimized HEO–$NaBH_4$ electrode fabricated in this work exhibits highly competitive performance relative to similar materials, as summarized in Table S3 in the ESM. Thus, the HEO–$NaBH_4$ electrode exhibits superior electrochemical performance even though it has a lower specific surface area than HEO–H_2O_2 and pristine HEO and nearly identical lattice distortion to HEO–H_2O_2. Thus, the enhancement is mainly attributed to the high O_V concentration, not to lattice distortion or textural effects.

3.3 Kinetic analysis

To understand the underlying mechanism of performance enhancement by oxygen vacancies, detailed electrochemical kinetic studies are performed. Figure 5(a) shows the initial EIS spectra of the three as-synthesized electrodes. HEO–$NaBH_4$ demonstrates the smallest semicircle diameter in the high-frequency region, implying the lowest charge transfer resistance (R_{ct}). Correspondingly, in the low-frequency region, it also shows the smallest slope of the line, reflecting accelerated Li^+ diffusion and improved mass transport at the electrode–electrolyte interface. These combined characteristics enable efficient charge transfer across the electrode–electrolyte interface and consequently accelerate the overall reaction.

CV curves of all three electrodes are recorded at scan rates ranging from 0.1 to 1.0 mV·s^{-1} (Fig. 5(b) and Figs. S6(a) and S7(a) in the ESM). The total charge storage (integral area) can be deconvoluted into two parts: surface capacitive-controlled behavior and solid-phase diffusion-controlled processes. Based on the linear relationship between the peak current (i_p) and the scan rate (v), $\lg i_p = \lg a + b\lg v$, the calculated b values are in the range of 0.80–0.83 (Fig. 5(c) and Figs. S6(b) and S7(b) in the ESM), indicating that the lithium storage behavior in all three electrodes is governed by a combination of pseudocapacitive and diffusion-controlled behavior. The capacity contribution can be further quantified by the equation $i(V) = k_1v + k_2v^{1/2}$, where k_1v and $k_2v^{1/2}$ represent the pseudocapacitive and diffusion-controlled processes, respectively [10]. The calculated pseudocapacitive contributions are plotted as a function of scan rates (Figs. 5(d) and 5(e), and Figs. S6(c), S6(d), S7(c), and S7(d) in the ESM), with the results summarized in Fig. 5(f). After the reduction treatments, both the

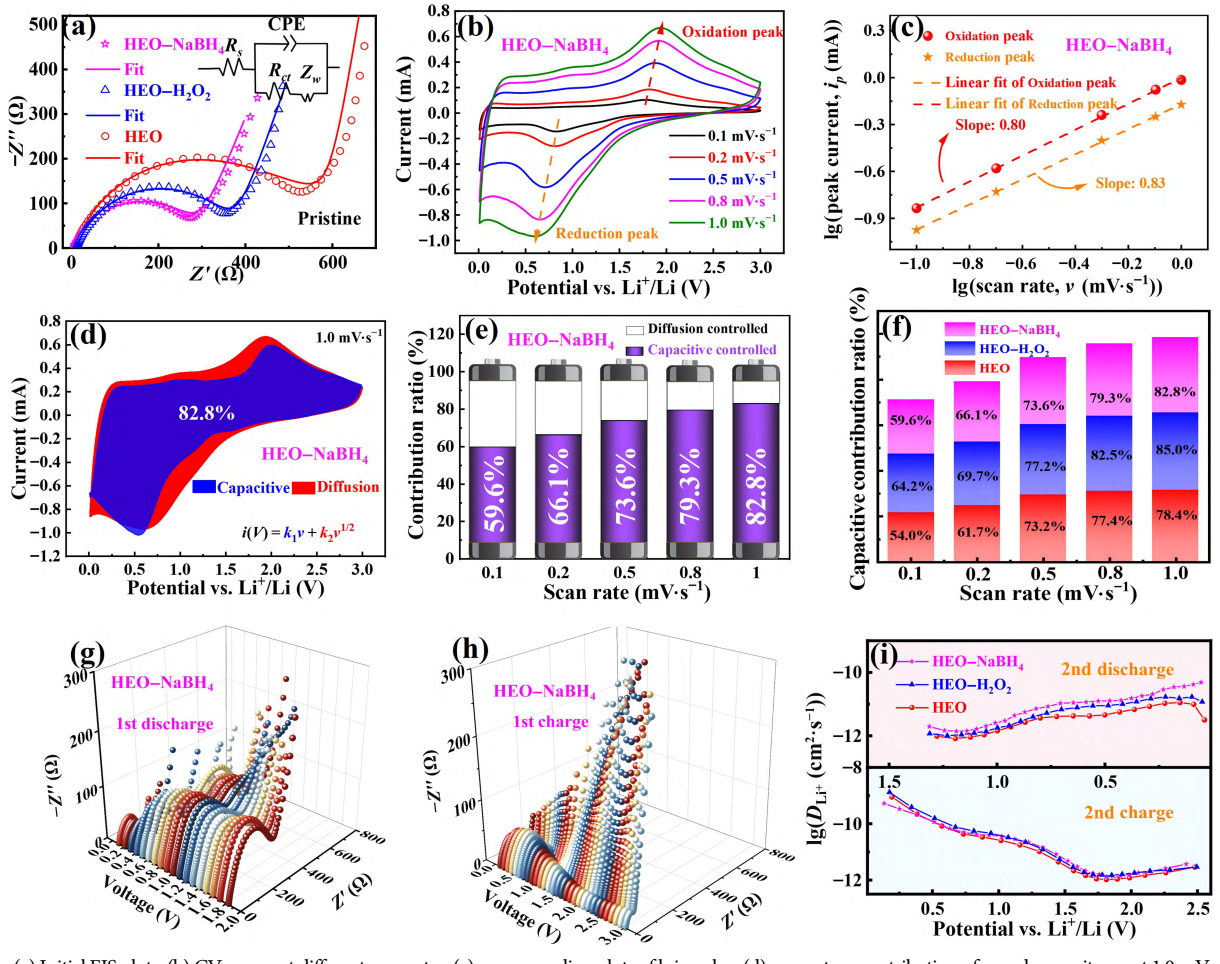

Fig. 5 (a) Initial EIS plots; (b) CV curves at different scan rates, (c) corresponding plots of lgi_p vs. lg$v$, (d) percentage contribution of pseudocapacitance at 1.0 mV·s^{-1}, and (e) capacitive contribution ratio at different scan rates of HEO–$NaBH_4$; (f) capacitive contribution ratios at different scan rates for all three electrodes; (g, h) *in situ* EIS spectra of HEO–$NaBH_4$ electrode upon first cycling; and (i) Li^+ diffusion coefficients from GITT for all three electrodes.

HEO–$NaBH_4$ and HEO–H_2O_2 electrodes exhibit higher pseudocapacitive contributions than the pristine HEO at identical scan rates. Specifically, the pseudocapacitive contribution of the HEO–$NaBH_4$ electrode rises from 59.6% at 0.1 mV·s^{-1} to 82.8% at 1.0 mV·s^{-1}, while that of the HEO–H_2O_2 electrode increases from 64.2% to 85.0%. The higher pseudocapacitive contribution of HEO–H_2O_2 over HEO–$NaBH_4$ is not due to oxygen vacancies but rather to its superior textural properties, namely, a larger specific surface area that offers more accessible sites for surface-driven charge storage.

The migration resistance of electron/Li^+ in all three electrodes is further compared by *in situ* EIS during the first cycle, with the results presented in Figs. 5(g) and 5(h), and Figs. S8(a)–S8(d) in the ESM. As shown in Figs. 5(g) and 5(h), R_{ct} decreases progressively with cycling, which can be attributed to electrochemical activation-induced grain refinement that creates additional pathways for Li^+ transport. In the first discharge to 1 V, a new semicircle appears in the high-frequency region, indicating the initial formation of an SEI layer on the electrode surface, which corresponds well with the sharp reduction peak observed in the first-cycle CV curve. Upon subsequent charging to 1 V, this SEI-related semicircle disappears, suggesting that the initially formed SEI layer is metastable and likely undergoes structural reorganization. Furthermore, EIS spectra collected at representative cutoff voltages (Fig. S9 in the ESM) clearly show that the R_{ct} of HEO–$NaBH_4$ is the smallest, followed by HEO–H_2O_2 and then pristine HEO. This trend confirms that reduction treatments effectively enhance the charge-transfer kinetics at the electrode–electrolyte interface.

In addition, the Li^+ diffusion coefficients (D_{Li^+}) of the three electrodes were determined using the GITT technique (Fig. S10 in the ESM). According to the GITT results (Fig. 5(i)), the HEO–$NaBH_4$ electrode exhibits the highest D_{Li^+} during the discharge process, which can be attributed to its higher concentration of O_V. The liquid-phase reduction induces structural distortion, which widens Li^+ transport channels and increases diffusion pathways, particularly at low current densities. Furthermore, these lattice distortions act as redox-active sites, further enhancing the Li^+ storage performance. The uneven charge distribution around these vacancies generates an internal electric field, which provides additional Coulombic attraction for Li^+, thereby facilitating its diffusion. In contrast, during the charge process, the variation in D_{Li^+} among the three electrodes is relatively small [38].

To further investigate the structural evolution of the HEO–$NaBH_4$ electrode upon extended cycling, *in situ* EIS analysis was performed after 200 and 300 cycles at 0.2 A·g^{-1}, as shown in Fig. S11 in the ESM. Clearly, R_{ct} progressively decreases from 200 to 300 cycles, confirming continuous activation of the electrode material. This sustained activation leads to a lower R_{ct} compared with the pristine state, accounting for the increasing capacity observed at 0.2 A·g^{-1}. Moreover, after 300 cycles, the EIS spectra

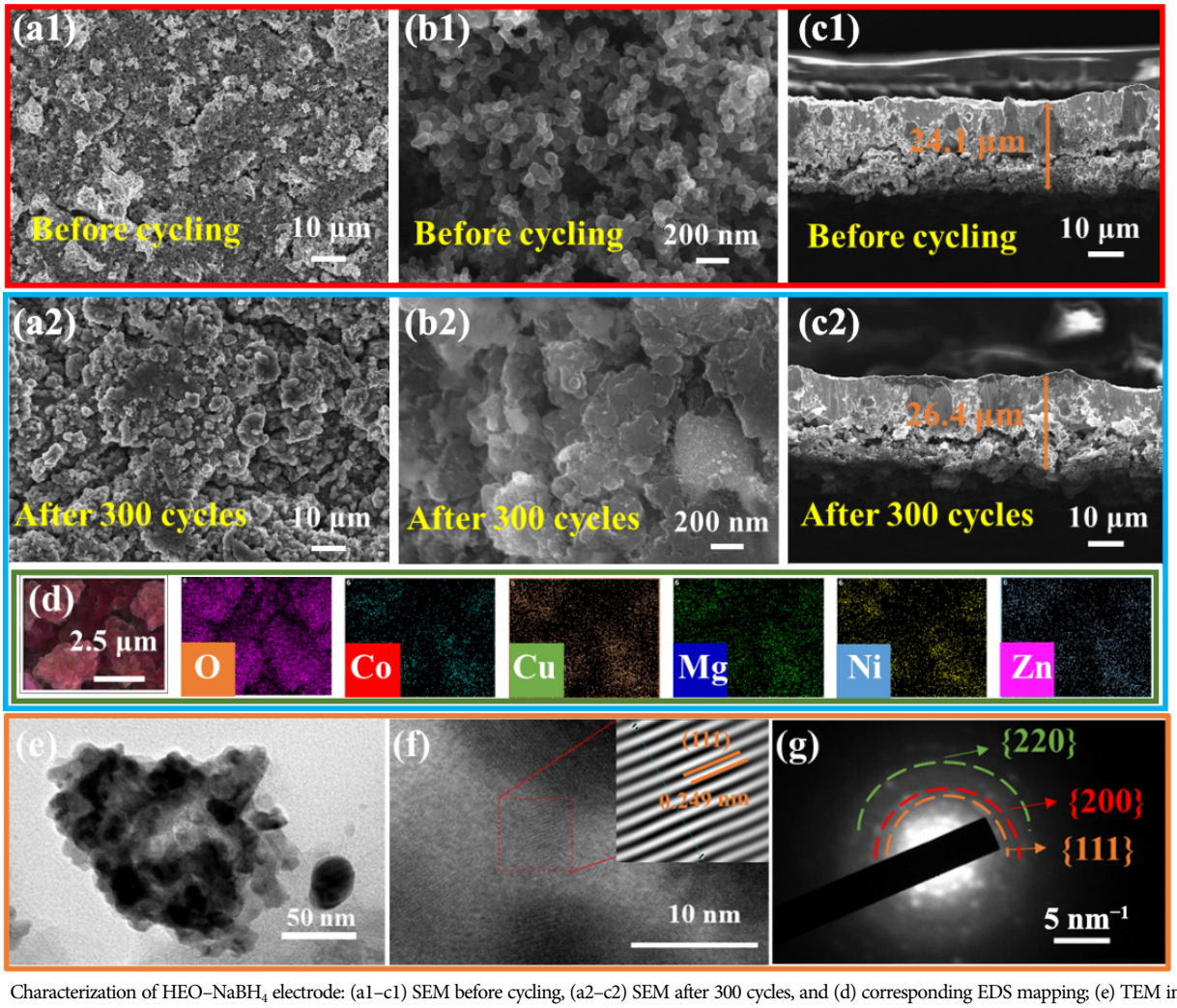

Fig. 6 Characterization of HEO–$NaBH_4$ electrode: (a1–c1) SEM before cycling, (a2–c2) SEM after 300 cycles, and (d) corresponding EDS mapping; (e) TEM images, (f) HRTEM image, and (g) SAED pattern after 300 cycles.

show negligible variation across different voltage states, indicating that a dense and homogeneous SEI layer has been maintained.

Furthermore, SEM images of the HEO–$NaBH_4$ electrode surface before cycling (Figs. 6(a1) and 6(b1)) and after 300 cycles (Figs. 6(a2) and 6(b2)) reveal notable particle agglomeration and grain refinement phenomena. EDS elemental mapping further shows a uniform element distribution of all constituent elements, supporting the robust structural stability of the active material. Meanwhile, cross-sectional SEM analysis (Figs. 6(c1) and 6(c2)) indicates that the thickness of the HEO–$NaBH_4$ electrode sheet increases from 24.1 to 26.4 μm after 300 cycles, corresponding to a volume expansion of 9.5%. This value is significantly lower than the 15%–20% expansion reported for a rock-salt $(Co_{0.2}Cu_{0.2}Mg_{0.2}Ni_{0.2}Zn_{0.2})O$ anode prepared via a salt-assisted strategy after merely 100 cycles [39].

Moreover, the active materials after 300 cycles were also analyzed by TEM (Figs. 6(e) and 6(f)). The TEM image (Fig. 6(e)) confirms the formation of ultrafine grains, while the distinct lattice fringes in the HRTEM image (Fig. 6(f)) and partial diffraction rings in the SAED pattern (Fig. 6(g)) unambiguously demonstrate that the rock-salt host structure is retained even after prolonged cycling. Notably, a clear increase in the (111) interplanar spacing is observed, from 2.38 Å in the pristine state (Fig. 2(g)) to 2.49 Å after 300 cycles (Fig. 6(f)), which is likely induced by the irreversible incorporation of Li^+ into the lattice. Collectively, the observed smaller volume expansion, grain refinement, and preserved rock-salt structure after 300 cycles confirm the enhanced capacity and cycling stability of the HEO–$NaBH_4$ electrode. Based on literature, this superior structural stability originates from the formation of a mesocrystal architecture during lithiation, which preserves the fundamental rock-salt structure framework [40]. This intermediate phase subsequently acts as a structural template during delithiation, facilitating the reconstruction of the rock-salt lattice and thereby ensuring the structural integrity of HEOs through repeated charge–discharge cycles.

4 Conclusions

This work demonstrates that defect engineering via a liquid reduction treatment effectively enhances the electrochemical performance of rock-salt-type $(Co_{0.2}Cu_{0.2}Mg_{0.2}Ni_{0.2}Zn_{0.2})O$ HEO anodes. Synthesized by SCS and subsequently reduced with H_2O_2 and $NaBH_4$ solution, the oxygen-deficient HEOs maintain a single-phase structure with refined crystallites, tuned porosity, and slightly increased lattice distortion, which collectively narrow the band gap and boost conductivity. Enabled mainly by the introduced oxygen vacancies (charge compensated mainly by Co and Ni) and optimized microstructure, the HEO–$NaBH_4$ electrode delivers a high reversible capacity of 802 $mAh{\cdot}g^{-1}$ after 300 cycles at 0.2 $A{\cdot}g^{-1}$ and retains 319 $mAh{\cdot}g^{-1}$ after 500 cycles at 1 $A{\cdot}g^{-1}$. Corresponding kinetic studies confirm lower R_{ct}, higher pseudocapacitive contribution, and faster D_{Li}^+, underscoring the crucial role of oxygen vacancies in facilitating electron/ion transport kinetics. Additionally, *in situ* and *ex situ* post-cycling characterizations demonstrate entropy-driven structural stability, which suppresses electrode volume expansion and ensures highly reversible reactions. These findings highlight the promise of defect-modulated HEOs and provide a valuable reference for designing advanced HEO anodes for LIBs.

Acknowledgements

This work was supported by the University Natural Science Research Project of Anhui Province, China (No. 2023AH051104), the Open Project of Anhui Province Key Laboratory of Efficient Conversion and Solid-State Storage of Hydrogen & Electricity (No. ECSSHE2024KF05), and the Natural Science Foundation of Henan Province (No. 262300421990).

Availability of data and materials

The data that support the findings of this study are available from the corresponding author upon reasonable request.

Competing interests

The authors have no competing interests to declare that are relevant to the content of this article.

Electronic Supplementary Material

Supplementary material is available in the online version of this article at https://doi.org/10.26599/JAC.2026.9221328.

References

[1] Lim H, Sung J, Jung JW, *et al.* Design and synthesis of advanced electrode materials: From Li-ion to Na-ion batteries. *Chem Commun* 2025, **61**: 16150–16169.

[2] Jia YP, Fan YB, Zhu J, *et al.* Research progress and standardization construction investigation of silicon carbon anode materials for lithium-ion batteries. *Adv Ceram* 2024, **45**: 408–416. (in Chinese)

[3] Wang QS, Liu XW, He DP, *et al.* Fundamental comprehension, synthetic procedures and catalytic applications of high entropy oxide nanomaterials. *Mater Today* 2023, **70**: 218–236.

[4] Sarkar A, Wang QS, Schiele A, *et al.* High-entropy oxides: Fundamental aspects and electrochemical properties. *Adv Mater* 2019, **31**: 1806236.

[5] Ouyang B, Zeng Y. The rise of high-entropy battery materials. *Nat Commun* 2024, **15**: 973.

[6] Duan LP, Du YC, Liu YJ, *et al.* Recent advances in high-entropy materials for efficient alkali metal-ion batteries. *Chem Soc Rev* 2025, **54**: 11740–11826.

[7] Huang LP, Zhu JT, Liu JX, *et al.* Emerging high-entropy strategy: A booster to the development of cathode materials for power batteries. *J Adv Ceram* 2024, **13**: 1093–1118.

[8] Bao MF, Wei ZB, Xu SB, *et al.* Temperature-mediated crystallinity engineering in spinel high-entropy oxide anode enable high-rate pseudocapacitive lithium-ion storage. *J Power Sources* 2026, **661**: 238632.

[9] Chen SJ, Bao MF, Jia YG, *et al.* Lattice distortion induced rock salt high-entropy oxide for high-rate lithium-ion storage. *J Alloy Compd* 2024, **990**: 174480.

[10] Liu XF, Ding LX, Li KZ, *et al.* The role of oxygen defects in high entropy perovskite for lithium ion batteries. *Acta Mater* 2025, **287**: 120812.

[11] Liu XF, Xing YY, Xu K, *et al.* Kinetically accelerated lithium storage in high-entropy (LiMgCoNiCuZn)O enabled by oxygen vacancies. *Small* 2022, **18**: 2200524.

[12] Osenciat N, Bérardan D, Dragoe D, *et al.* Charge compensation mechanisms in Li-substituted high-entropy oxides and influence on Li superionic conductivity. *J Am Ceram Soc* 2019, **102**: 6156–6162.

[13] Ozgur C, Erdil T, Geyikci U, *et al.* Engineering oxygen vacancies in $(FeCrCoMnZn)_3O_{4-\delta}$ high entropy spinel oxides through altering fabrication atmosphere for high-performance rechargeable zinc-air batteries. *Glob Chall* 2024, **8**: 2300199.

[14] Zhong MX, Xu TT, Wang C, *et al.* Utilizing high entropy oxide $(Ni_{0.2}Co_{0.2}Ca_{0.2}Cu_{0.2}Mg_{0.2})Fe_2O_4$ in chemical looping process for highly efficient and stable hydrogen production. *Chem Eng J* 2024, **487**: 150521.

[15] Gu KZ, Wang DD, Xie C, *et al.* Defect-rich high-entropy oxide nanosheets for efficient 5-hydroxymethylfurfural electrooxidation. *Angew Chem Int Edit* 2021, **60**: 20253–20258.

[16] Zhang DY, Feng BH, Guo WB, *et al.* Formation of surfaces oxide

vacancies in porous $ZnCo_2O_4$ nanoflowers for enhanced energy storage performance. *Discov Nano* 2025, **20**: 156.
[17] Wang K, Hua WB, Huang XH, *et al.* Synergy of cations in high entropy oxide lithium ion battery anode. *Nat Commun* 2023, **14**: 1487.
[18] Li XP, Miao KK, Guo SF, *et al.* Enhanced catalytic activity of ZnO–CuO–Co_3O_4 composites achieved using a mechanochemical method for effective Fenton-like dye removal: The generation and catalytic mechanism of various superficial active sites. *Mater Adv* 2023, **4**: 4943–4953.
[19] Jin CQ, Wang YL, Dong HB, *et al.* A novel spinel high-entropy oxide $(Cr_{0.2}Mn_{0.2}Co_{0.2}Ni_{0.2}Zn_{0.2})_3O_4$ as anode material for lithium-ion batteries. *Inorganics* 2024, **12**: 198.
[20] Liang YH, Feng RH, Jin CQ, *et al.* Preparation and electrochemical properties of high-entropy oxide $Li_x(CrMnCoNiZn)_{3-x}O_4$. *Mater Today Commun* 2025, **47**: 113111.
[21] Bao MF, Chen SJ, Xie HX, *et al.* Hollow/mesoporous spherical La$(Cr_{0.2}Fe_{0.2}Co_{0.2}Ni_{0.2}Mn_{0.2})O_3$ high-entropy oxide anode toward ultrafast and stable lithium storage. *J Mol Struct* 2025, **1340**: 142496.
[22] Chen SJ, Bao MF, Jia YG, *et al.* Boosting high-rate Li-ion storage properties by La(III) ion doping in spinel $(Co_{0.2}Cr_{0.2}Fe_{0.2}Mn_{0.2}Ni_{0.2})_3O_4$ high-entropy oxide anode. *J Adv Ceram* 2024, **13**: 769–779.
[23] Yin ZQ, Mao YF, Shi SK, *et al.* Solution combustion synthesis of high-entropy rare earth oxide $Ce_{0.2}La_{0.2}Gd_{0.2}Y_{0.2}Lu_{0.2}O_{1.6}$:$Eu^{3+}$phosphor with intense blue-light excitable red emission for solid-state lighting. *J Adv Ceram* 2024, **13**: 1852–1860.
[24] Berardan D, Meena AK, Franger S, *et al.* Controlled Jahn–Teller distortion in (MgCoNiCuZn)O-based high entropy oxides. *J Alloy Compd* 2017, **704**: 693–700.
[25] Yang XB, Wang HQ, Song YY, *et al.* Low-temperature synthesis of a porous high-entropy transition-metal oxide as an anode for high-performance lithium-ion batteries. *ACS Appl Mater Inter* 2022, **14**: 26873–26881.
[26] Wang RJ, Chen JR, Zhang YX, *et al.* Inhibiting phase conversion and improving cyclic stability of Ni-rich layered oxide by high-valence element concentration gradient doping. *Chem Eng J* 2024, **485**: 149827.
[27] Patra J, Nguyen TX, Tsai CC, *et al.* Effects of elemental modulation on phase purity and electrochemical properties of Co-free high-entropy spinel oxide anodes for lithium-ion batteries. *Adv Funct Mater* 2022, **32**: 2110992.
[28] Tian KH, Duan CQ, Ma Q, *et al.* High-entropy chemistry stabilizing spinel oxide $(CoNiZnXMnLi)_3O_4$ (X = Fe, Cr) for high-performance anode of Li-ion batteries. *Rare Metals* 2022, **41**: 1265–1275.
[29] Xiao B, Wu G, Wang TD, *et al.* High entropy oxides $(FeNiCrMnX)_3O_4$ (X = Zn, Mg) as anode materials for lithium ion batteries. *Ceram Int* 2021, **47**: 33972–33977.
[30] Manohar A, Krishnamoorthi C. Site selective Cu^{2+} substitution in single crystal Fe_3O_4 biocompatible nanospheres by solvothermal reflux method. *J Cryst Growth* 2017, **473**: 66–74.
[31] Idriss H. On the wrong assignment of the XPS O1s signal at 531–532 eV attributed to oxygen vacancies in photo- and electro-catalysts for water splitting and other materials applications. *Surf Sci* 2021, **712**: 121894.
[32] Zheng H, Gu YH, Zhang DS, *et al.* (1–*x*)SBKT–*x*LMT lead-free ceramics with exceptional temperature stability and high energy density. *Chem Eng J* 2025, **512**: 162493.
[33] Jin YW, Huo WJ, Zhang LB, *et al.* $NaBH_4$-reduction induced tunable oxygen vacancies in $LaNiO_{2.7}$ to enhance the oxygen evolution reaction. *Chem Commun* 2021, **57**: 7168–7171.
[34] Zhang BZ, Chen J, Li Y, *et al.* Engineering of pore design and oxygen vacancy on high-entropy oxides by a microenvironment tailoring strategy. *Inorganic Chemistry* 2024, **63**: 5689-5700.
[35] Jia YG, Chen SJ, Shao X, *et al.* Synergetic effect of lattice distortion and oxygen vacancies on high-rate lithium-ion storage in high-entropy perovskite oxides. *J Adv Ceram* 2023, **12**: 1214–1227.
[36] Zhang ZQ, Lu SY, Huang G, *et al.* Carbon-coated $Li_4Ti_5O_{12}$ optimized by fluorine regulation strategy for high-rate lithium-ion batteries with mixed diffusion and capacitive effects. *Carbon* 2024, **221**: 118885.
[37] Su JY, Cao ZZ, Jiang ZP, *et al.* High entropy oxide nanofiber by electrospun method and its application for lithium battery anode material. *Int J Appl Ceram Tec* 2022, **19**: 2004–2015.
[38] Hou SS, Su L, Wang S, *et al.* Unlocking the origins of highly reversible lithium storage and stable cycling in a spinel high-entropy oxide anode for lithium-ion batteries. *Adv Funct Mater* 2023, **34**: 2307923.
[39] Liu XF, Wang HH, Dong L, *et al.* Molten salt synthesis, morphology modulation, and lithiation mechanism of high entropy oxide for robust lithium storage. *J Energy Chem* 2023, **86**: 536–545.
[40] Wang W, Song WJ, Li YS, *et al.* Mesocrystallinely stabilized lithium storage in high-entropy oxides. *Nano Energy* 2024, **124**: 109482.